Electrochimica Acta 441 (2023) 141865

Contents lists available at ScienceDirect

Electrochimica Acta

journal homepage: www.journals.elsevier.com/electrochimica-acta

Nanostructured europium-doped layered lithium manganese oxide as a prospective cathode material for aqueous lithium-ion battery

TumisoE Mabokela [a,b], Assumpta C Nwanya [a,c,*], Miranda M Ndipingwi [a,b], Sodiq T Yussuf [a,b], Precious I Ekwere [a,b], Onyinyechi V Uhuo [a,b], Chinwe O Ikpo [a,b], Kwena D Modibane [d], Emmanuel I Iwuoha [a,b,*]

[a] SensorLab, (University of the Western Cape Sensor Laboratories), 4th Floor Chemical Sciences Building, University of the Western Cape, Bellville 7535, Cape Town, South Africa
[b] DSI/NRF South African Research Chair for NanoElectrochemistry & Sensor Technology, University of the Western Cape, Bellville 7535, Cape Town, South Africa
[c] Department of Physics and Astronomy, University of Nigeria, Nsukka, Nigeria
[d] Nanotechnology Research Lab, Department of Chemistry, School of Physical and Mineral Sciences, University of Limpopo (Turfloop), Polokwane, South Africa

ARTICLE INFO

Keywords:
Batteries
Energy storage
Lithium-ion
Lithium rich manganese oxide
Perovskite
Rock Salt

ABSTRACT

As the world moves to greener and renewable energy generation technologies, scientific researchers are facing a great challenge of concurrently developing energy storage materials with a low production cost, environmentally benign, high-energy density, and good safety. In this work, we report on the improved cycling and reduced phase transformation of the well-studied n-Li_2MnO_3 achieved by doping with Europium. It was established from cyclic voltammetry results that Eu-doping had a stabilization effect on the lattice oxygen and further prevented the migration of the manganese ions previously coordinated to the released lattice oxygen, into vacant octahedral site that were occupied by the removed Li^+. As such, the new material exhibited an increase in conductivity with cycling and coulombic efficiency increased from ~74 to ~88% over 100 cycles. Moreover, the discharge capacity of $Li_2Mn_{0.95}Eu_{0.05}O_3$ improved with cycling from 4.20 mAh.g^{-1} to 5.47 mAh.g^{-1}.

1. Introduction

The global energy demand is increasing at an alarming rate due to the rapid increase in the global population [1,2]. This rapid rise in the global population is associated with mounting industrialization and urbanization activities which have greatly increased the global energy demand [3,4]. Currently, fossil fuel derived oil and gas play a major role in feeding this demand as estimates indicate that over 85% of the global energy demand is met by the burning of fossil fuels [5,6]. The use of fossil derived fuels to feed the ever-increasing demand for energy is becoming unsustainable and presents a myriad of environmental, economic, and health problems [7,8]. During the burning of fossil fuels, large amounts of greenhouse gases such as carbon dioxide (CO_2), methane (CH_4) and nitrous oxide (N_2O) are emitted into the atmosphere [9]. The elevated CO_2 emissions from this exercise are seen as the major contributor to global warming and climate change [10]. As a result of above-mentioned factors, there is a need to develop renewable and cleaner means of energy generation, to further mitigate climate change and environmental pollution associated with fossil fuel use.

To date, several renewable energy sources and technologies are being widely researched and developed as possible alternatives to the use of fossil derived fuels [11]. Examples include wind and solar energy which harness nature's clean energy, are promising candidates due to their reduced carbon footprint in contrast to their non-renewable counterparts [11]. Despite being cleaner and cheaper per unit energy than fossil fuel derived oil, wind and solar energy generation also have limitations [11,12]. The limitations lie in that the electricity generation is not constant but varies at different times and according to weather conditions [11]. Thus electrochemical/mechanical energy storage systems are pivotal for wide range adoption of renewable energy sources and integration into the grid [13,14].

Lithium-ion batteries have attracted a great deal of attention in the research and development of large grid and electric vehicle energy storage systems [14–17]. This is due to their higher specific energy, longer life span, power densities and their wide range of temperature versatility in applications [17,18]. However, currently available Li-ion

* Corresponding authors.
E-mail address: chinwe.nwanya@unn.edu.ng (A.C. Nwanya).

https://doi.org/10.1016/j.electacta.2023.141865
Received 24 August 2022; Received in revised form 28 November 2022; Accepted 7 January 2023
Available online 10 January 2023

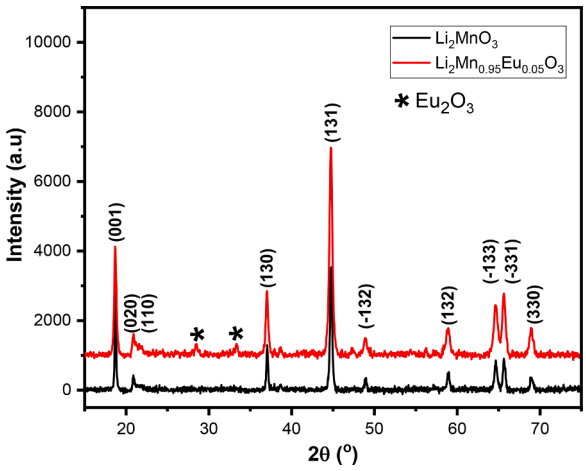

Fig. 1. The Powder X-ray Diffraction (PXRD) patterns of Li_2MnO_3 and $Li_2Mn_{0.95}Eu_{0.05}O_3$.

batteries cannot meet all the requirements for applications in electric vehicles and electrical grid storage systems. These include low production cost, environmentally benign, high-energy density, and good safety [19]. For example, the best performing commercial Li-ion battery consists of a cobalt based cathode ($LiCoO_2$) which is both costly and toxic [19,20]. The limiting factor to higher capacity and performance in Li-ion batteries is the relatively low capacities of their cathode materials ($LiCoO_2$, $LiNiO_2$, $LiMn_2O_4$, $LiFePO_4$ and $LiMnO_2$) with specific capacities ranging from 100 to 180 mA h g^{-1} [21,22].

Li_2MnO_3 has gained attraction as a possible cathode material in rechargeable lithium-ion batteries due to its low cost [22,23], high theoretical capacity [24] and non-toxicity [25,26]. However, this promise is overshadowed by the material's low conductivity [27], capacity fading with cycling, phase transformation [28] and poor rate capability [28]. Doping has been reported as an effective strategy to improve the performance of Li_2MnO_3 [29], but much focus has been put on doping using ordinary transition metals such as Na [29], Mg [30], Al [31], Ni [32], Mo [33] and Ti [34]. Recently, several researchers [35–38] have drifted their attention to doping cathode materials with rare earth elements with great success. However, to our knowledge, very few publications [39–41] have reported on rare earth element doping of Li_2MnO_3. Herein, we report on the effects of Eu-doping on the physico-chemical and electrochemical properties of Li_2MnO_3.

2. Experimental

2.1. Preparation of Li_2MnO_3

All reagents used in this study were AnalaR Grade chemicals supplied by Merck, Johannesburg, South Africa. Briefly, 2.263 g of $LiOOCCH_3$ and 4.198 g $Mn(OOCCH_3)_2{\cdot}4H_2O$ were dissolved in 50 ml of ultra-pure distilled water, respectively. The two salt solutions were stirred for 10 min independently before mixing in a 250 ml round bottom flask. 14.904 g EDTA and 2.874 ml of ethylene glycol $(CH_2OH)_2$ were added to the mixture with further magnetic stirring for 15 min forming a white suspension. To the resulting white suspension, 35 ml of NH_4 were added drop wise to adjust the pH to 12. At the adjusted pH of 12, a clear solution resulted and was then heated to 80 °C under vigorous stirring overnight to yield a viscous gel. The resulting gel was oven dried at 80 °C for 12 h before sintering. The dried gel was first calcined at 450 °C with a ramping rate of 5 °C/min for 2 h to remove all organic components, followed by intermediate grinding, then heated to 750 °C for 8 h to obtain 1.73 g of the brick red Li_2MnO_3 product.

2.2. Preparation of $Li_2Mn_{0.95}Eu_{0.05}O_3$

Briefly, 1.621 g of $LiOOCCH_3$, 0.264 g $Eu(NO_3)_3{\cdot}5H_2O$ and 2.872 g $Mn(OOCCH_3)_2{\cdot}4H_2O$ were dissolved in 50 ml of ultra-pure distilled water, respectively. The three salt solutions were stirred for 10 min independently before mixing in a 250 ml round bottom flask. 10.788 g EDTA and 2.643 ml of $(CH_2OH)_2$ were added to the mixture with further magnetic stirring for 15 min forming a white suspension. To the resulting white suspension, 35 ml of NH_4 were added drop wise to adjust the pH to 12. At the adjusted pH of 12, a clear solution resulted and was then heated to 80 °C under vigorous stirring overnight to yield a viscous gel. The resulting gel was oven dried at 80 °C for 12 h before sintering. The dried gel was first calcined at 450 °C with a ramping rate of 5 °Cmin^{-1} for 2 h to remove all organic components, followed by intermediate grinding. The resulting powder was then heated to 750 °C for 8 h to obtain 1.89 g of the brick red $Li_2Mn_{0.95}Eu_{0.05}O_3$ product.

2.3. Characterization

Diffraction measurement for crystallinity and phase identification of Li_2MnO_3 and $Li_2Mn_{0.95}Eu_{0.05}O_3$ were performed using Bruker AXS D8 Advanced X-Ray Diffractometer (XRD) (Bruker, Billerica, MA, USA) with a Bruker LYNXEYE detector using Cu $K\alpha_1$ =1.5406 Å radiation. The measurements were run in the 10 - 80 2θ range with a typical step size of 0.034° High Resolution Transmission Electron Microscope (HR-TEM) for morphology, crystallite size and crystallinity studies were obtained using FEI Tecnai G^2 F20 (Field Electron and Ion Company (FEI) Europe, Eindhoven, The Netherlands). A Zeiss Auriga Scanning Electron Microscope (Carl Zeiss Microscopy GmbH, Jena, Germany). High Resolution Scanning Electron Microscope (HR-SEM) with Electron Dispersive Spectroscopy (EDS), was used to determine surface morphology, elemental composition, shape, and distribution. For functional group identification of the Li_2MnO_3 and $Li_2Mn_{0.95}Eu_{0.05}O_3$, Fourier Transform Infrared Spectroscopy (FT-IR) was performed using PerkinElmer Spectrum 100 Spectrometer (PerkinElmer Incorporated, Shelton, CT, USA) via the KBr pellet sample preparation method. Particle size and shape analysis of the synthesised materials were determined by Small Angle X-Ray Scattering (SAXS) Spectroscopy using Anton Paar SAXSpace Spectrometer (Anton Paar, Graz, Austria).

2.4. Electrode fabrication

Nickel foam current collector (1 × 0.5 cm) was pre-treated to remove the nickel oxide (NiO) layer by firstly sonicating in 3 M hydrochloric acid (HCL) for 15 min, subsequently followed by sonication in distilled water and ethanol for a further 15 min each. The treated nickel foam was then oven dried overnight at 70 °C to evaporate any moisture or ethanol remaining in the foam. An area of 0.5 × 0.5 cm of the prepared nickel foam was depressed using a spatula to form a flat area and was coated with an electrode material slurry prepared by mixing 70% active material, 20% carbon black and 10% solution of 5 wt% PVDF-NMP to form the working electrode. The prepared electrode was then dried overnight at 70 °C.

2.5. Electrochemical characterization

All electrochemical studies of $Li_2Mn_{0.95}Eu_{0.05}O_3$ were performed using a biologic (Seyssinet-Pariset, France) VMP-300 potentiostat with EC-lab as the data acquisition software. For three-electrode configuration, the prepared n-Li_2MnO_3 electrode was used as the working electrode, platinum (Pt) wire as the counter electrode and silver-silver chloride (Ag/AgCl) as the reference electrode. Cyclic voltammetry (CV) studies were carried out at 10, 20, 50 and 100 mV.s^{-1} scan rates within the potential range −1 to 1 V in 1 M Li_2SO_4 electrolyte solution. For charge/discharge studies, the cells were charged to 1 V at 1.0 A.g^{-1} current density. Electrochemical Impedance Spectroscopy (EIS) studied were performed at a potential of 0.1295 V, amplitude of 5 mV and frequency range of 100 mHz to 100 kHz.

Table 1
Rietveld refinement results for Li_2MnO_3 and $Li_2Mn_{0.95}Eu_{0.05}O_3$ materials.

Crystal Data	Li_2MnO_3 (ICSD CIF file)	Li_2MnO_3	$Li_2Mn_{0.95}Eu_{0.05}O_3$
Space group	C2/c	C2/c	C2/c
a (Å)	4.928	4.927	4.936
b (Å)	8.533	8.535	8.562
c (Å)	9.604	9.592	9.610
α, γ (°)	90	90	90
β (°)	99.5	99.438	99.603
Vol ($Å^3$)	398.316	397.932	399.113
Density ($g.cm^{-3}$)	3.896	3.887	3.891

3. Results and discussion

3.1. Crystallographic characterization

The PXRD patterns of pristine and Eu-doped Li_2MnO_3 are given in Fig. 1. Both materials are indexed to a monoclinic system with a C2/c space group (JCP2 2–1252), with minor impurity peaks of Eu_2O_3 (JCP2 74–1988) observed in $Li_2Mn_{0.95}Eu_{0.05}O_3$ due to moderate ($x \geq 0.05$) dopant concentration [39]. The PXRD pattern of $Li_2Mn_{0.95}Eu_{0.05}O_3$ is further characterized by noise, which is a well reported phenomenon and can be attributed to oxygen removal, defects during annealing or defects due to substitution [40]. Furthermore, the patterns exhibit the characteristic super lattice peaks at 20–25° 2-theta angles corresponding to the Li/Mn ordering within the transition metal layers of the Li_2MnO_3 material indicating successful synthesis of the materials [42–45].

Rietveld refinement analyses of Li_2MnO_3 and $Li_2Mn_{0.95}Eu_{0.05}O_3$ powder XRD data were performed using the general structure analysis system (GSAS) II by Toby and Von Dreele [46]. The background, cell parameters, microstrain and size were all refined. The CIF file reported by Jansen and Hoppe [47] obtained from ICSD was used for the phase information. The starting unit cell parameters were at $a = 4.928$, $b = 8.533$ and $c = 9.604$. The Rietveld refinement results are presented in Table 1. The cell parameters were observed to increase in the $Li_2Mn_{0.95}Eu_{0.05}O_3$ sample, further confirming the presence of defects (size mismatch) induced by europium doping. The refined plots are shown in the supplementary information (Fig S1 and S2).

Fig. 2(a) shows the expanded PXRD patterns of Li_2MnO_3 and $Li_2Mn_{0.95}Eu_{0.05}O_3$ in the super lattice 2-theta region. The $Li_2Mn_{0.95}Eu_{0.05}O_3$ PXRD pattern in Fig. 2(a) shows expansion of the super lattice peak which suggested that the Eu-doping improved the ordering of the transition metal layer which could improve the stability of the superstructure [45]. Furthermore, evidence of doping is observed by the slight movement of the (001) peak as shown in Fig. 2(b) to lower 2-theta angles [44]. The shift to lower angles also suggests that Eu- ions expanded the cell volume of the lattice due to partial replacement of Mn^{4+} (0.67 Å) with Eu^{3+} (10.87 Å) which may lead to broadening of Li-ion diffusion

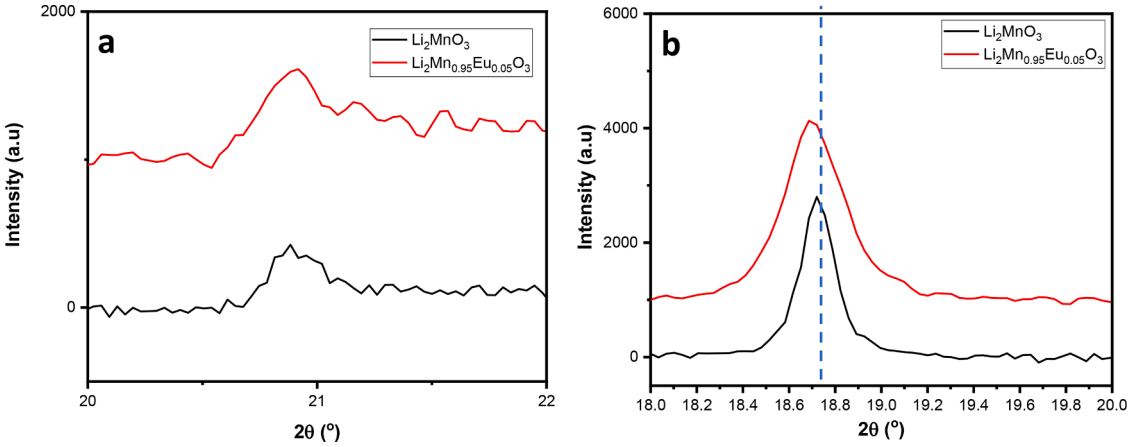

Fig. 2. (a) and (b) Expanded PXRD patterns of pristine Li_2MnO_3 and $Li_2Mn_{0.95}Eu_{0.05}O_3$.

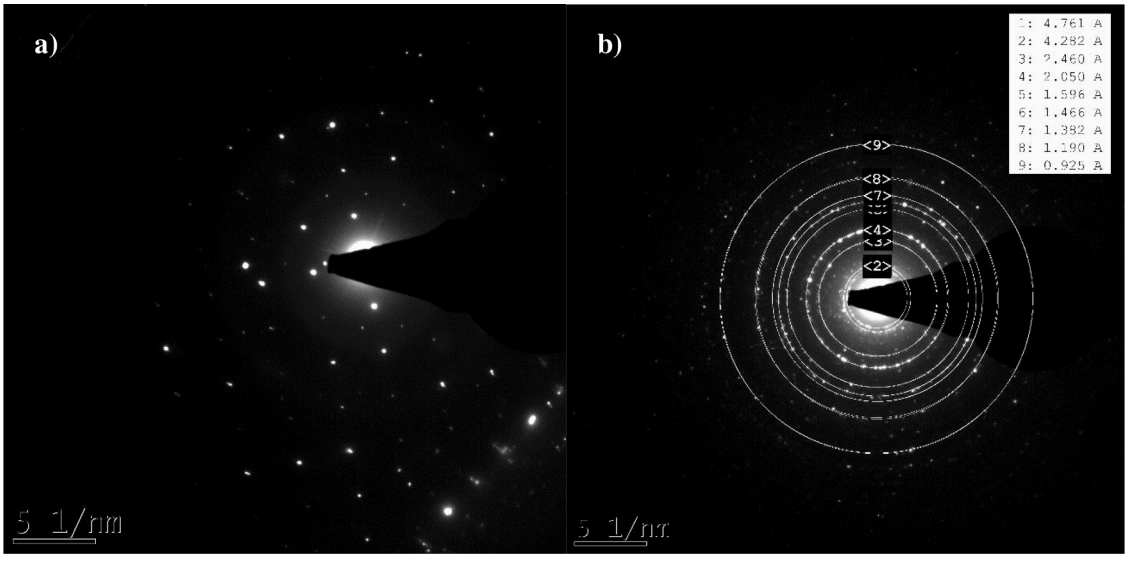

Fig. 3. SAED images of a) Li_2MnO_3 and b) $Li_2Mn_{0.95}Eu_{0.05}O_3$.

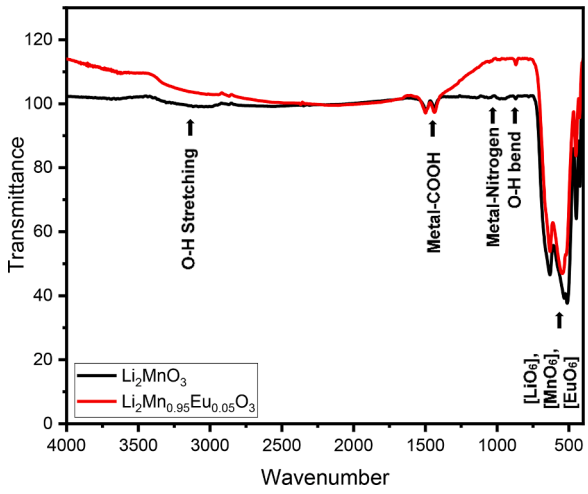

Fig. 4. FTIR spectra of Li_2MnO_3 and $Li_2Mn_{0.95}Eu_{0.05}O_3$.

pathways [44]. By using PXRD data, the average crystallite size of both materials was calculated using the Scherrer Debye Eq. (1) [39]:

$$D = \frac{k\lambda}{\beta \mathrm{Cos}\theta} \quad (1)$$

where D is the average crystallite size, k is the Scherrer constant (0.90), λ is the wavelength of X-ray radiation (Cu Kα_1 = 1.5406 Å), θ is the Bragg angle is radians and β is the full width half maximum of the diffraction peak in radians. From the Scherrer-Debye equation, the average crystallite sizes decreased from 28.32 to 19.05 nm with Eu doping of Li_2MnO_3.

The decrease in average crystallite size was attributed to particle growth restriction due to the lattice distorting effects of partial replacement of Mn^{4+} (0.67 Å) with Eu^{3+} (10.87 Å) and has been previously observed by other authors [48].

To further investigate the crystallinity of Li_2MnO_3 and $Li_2Mn_{0.95}Eu_{0.05}O_3$, the SAED technique was used. From the obtained SAED pattern of Li_2MnO_3 in Fig. 3(a), we clearly see that the pristine material exhibits a mono crystalline pattern and high phase purity. On the other hand, the SAED pattern of $Li_2Mn_{0.95}Eu_{0.05}O_3$ in Fig. 3(b) is of poly-crystalline nature, and all the rings can be indexed to the c2/c symmetry and monoclinic system. Furthermore, the D-spacings for each ring were calculated using *Image J* software and the values corresponded to (001), (020), (20–1), (131), (220), (132), (202), (330) and (311) hkl reflections of the Li_2MnO_3 phase. This indicated that $Li_2Mn_{0.95}Eu_{0.05}O_3$ maintained the structure of Li_2MnO_3, with its poly-crystalline nature indicating the presence of another phase i.e., Eu_2O_3 which is in good agreement with the PXRD data.

3.2. Spectroscopic characterization

Fig. 4 represents the FTIR spectra of Li_2MnO_3 and $Li_2Mn0.95Eu_{0.05}O_3$. FTIR spectroscopy was employed for functional groups identification of the synthesized materials. In both FTIR spectra, the appearance of peaks in the frequency range 420 - 650 cm^{-1} and ~1087 cm^{-1} are attributed to octahedrally coordinated metals i.e., Li, Mn and Eu [49]. The narrow peaks situated at ~870 cm^{-1} are assigned to the coordination of the Li, Mn, and Eu cations to the nitrogen functionality due to EDTA present in the material [48]. Furthermore, two broad peaks situated at the frequency range ~1427–1505 cm^{-1} are assigned to the coordination of the

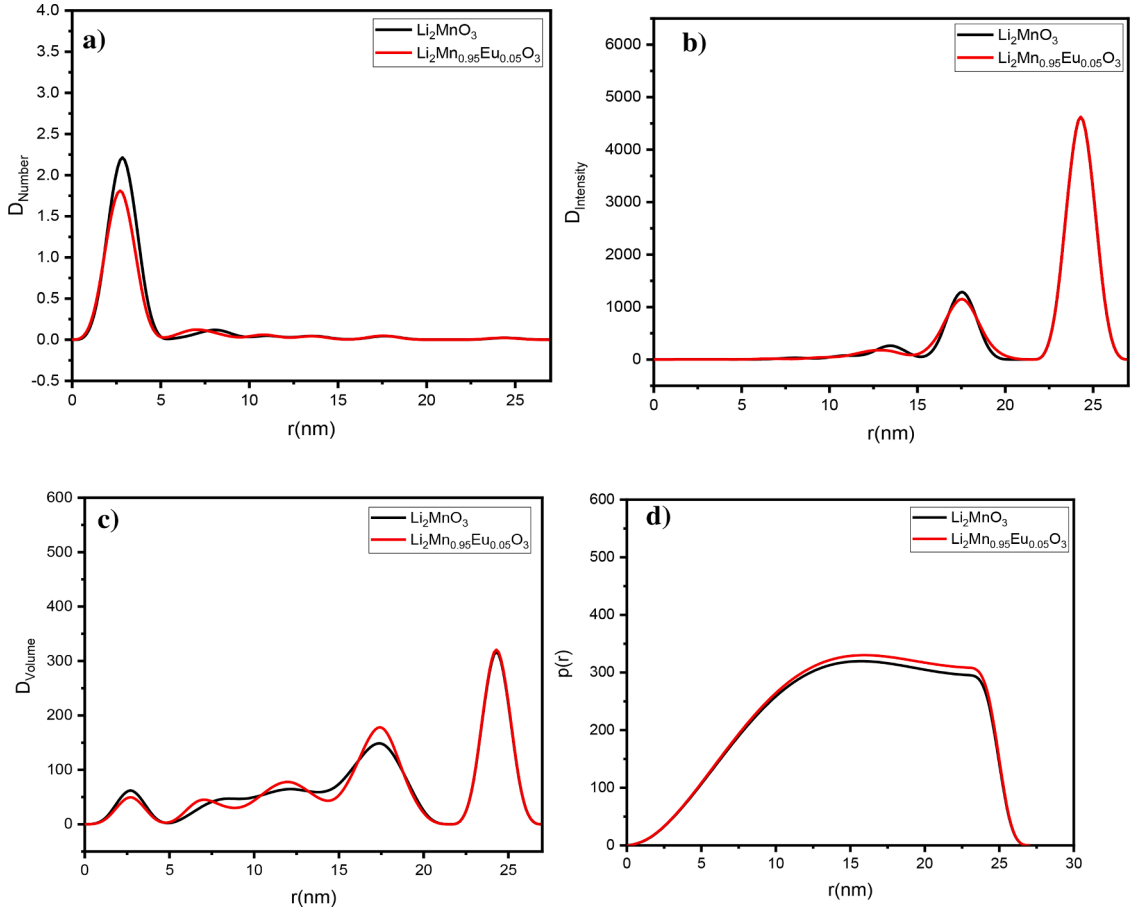

Fig. 5. SAXS plots of Li_2MnO_3 and $Li_2Mn_{0.95}Eu_{0.05}O_3$.

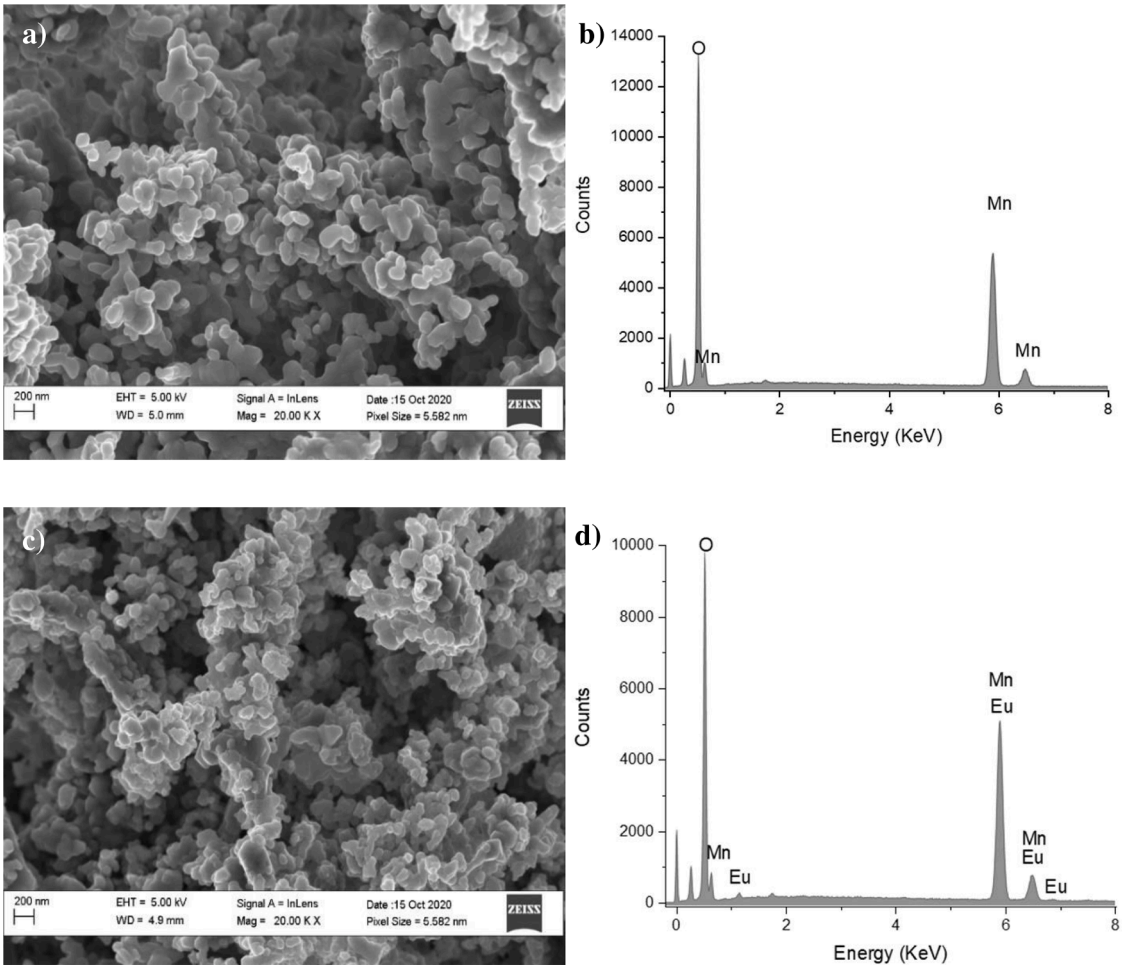

Fig. 6. HR-SEM images of a) Li_2MnO_3 and c) $Li_2Mn_{0.95}Eu_{0.05}O_3$ at 20.00 K X Magnification. EDX spectra of b) Li_2MnO_3 and d) $Li_2Mn_{0.95}Eu_{0.05}O_3$.

Table 2
EDX data of Li_2MnO_3 and $Li_2Mn_{0.95}Eu_{0.05}O_3$.

Sample	Concentration Weight%			Atomic%		
	Mn	Eu	O	Mn	Eu	O
Li_2MnO_3	63.10	–	36.9	33.2	0.0	66.8
$Li_2Mn_{0.95}Eu_{0.05}O_3$	62.68	2.71	34.61	34.3	0.5	65.1

carboxylic functionalities of EDTA to Li, Mn, and Eu cations [50]. The larger broad peak situated at ~3500 cm^{-1} is assigned to surface absorbed moisture. Both spectra show no variation, and no impurity peaks were found, which shows good synthesis and purity of the synthesized materials.

Fig. 5 represents the SAXS distribution curves of intensity, number, volume, and the free model PDDF of Li_2MnO_3 and $Li_2Mn_{0.95}Eu_{0.05}O_3$. Fig. 5(a) represents the distribution by number curves, which gives information about the number of the present primary particle sizes. From the data, most primary particles have an average radius of ≤ 5 nm (≤ 10 nm particle size). In Fig. 5(b), we observe distribution by intensity curves which informs us about self assembles within the materials. We observe that both samples exhibited particles assembling to form particles with radii of ~13 nm, ~17 nm and ~25 nm with the latter showing the highest intensity. This indicates that majority of particles assemble to form secondary particles of an average particle radius of ~25 nm (~54 nm particle size). Distribution by volume curves in Fig. 5 (c) give information of the present particle sizes in the materials.

In both samples, the present particle radii can be grouped into ≤ 5 nm, 5–20 nm and ~25 nm with the latter having the highest number of particles. The free model PDDF of both Li_2MnO_3 and $Li_2Mn_{0.95}Eu_{0.05}O_3$ in Fig. 5(d) shows a hybrid type shape, which could be an indication of the presence of both solid and hollow spheres as seen in Fig. 5(d). Furthermore, the hollow sphere particles appear at ~27 nm indicating that they have larger particle sizes (~50 nm). On the other hand, the average particle radius of all the particles is ~ 15 nm which suggests that the average particle size is ~30 nm.

3.3. Morphological characterization

The HR-SEM micrograph of Li_2MnO_3 and $Li_2Mn_{0.95}Eu_{0.05}O_3$ are shown in Fig. 6(a) and (c) respectively. It is well established that the morphology of fine powders is influenced by the choice of reagents, the method of preparation, synthesis, and calcining temperature [30,50]. Both images of Li_2MnO_3 and $Li_2Mn_{0.95}Eu_{0.05}O_3$ exhibit some agglomeration of smaller primary particle to form larger secondary particles. This is expected due to the low temperature synthesis method [30,31], the high surface free energy of the particles [45] and the use of EDTA as a chelating agent during synthesis [50]. EDTA has 6 active sites (two amino & four carboxyl groups) which strongly and actively binds to metal ions [50].

As a result of this strong connection between metal ions and EDTA, nucleation and growth are more controlled and particle size uniformity is achieved [50]. However, $Li_2Mn_{0.95}Eu_{0.05}O_3$ shows a higher-level of particle size uniformity, shape uniformity and a decrease in the size of the secondary particles when compared to Li_2MnO_3. This has been observed in numerous reports [30,44,45,48] on doped cathode

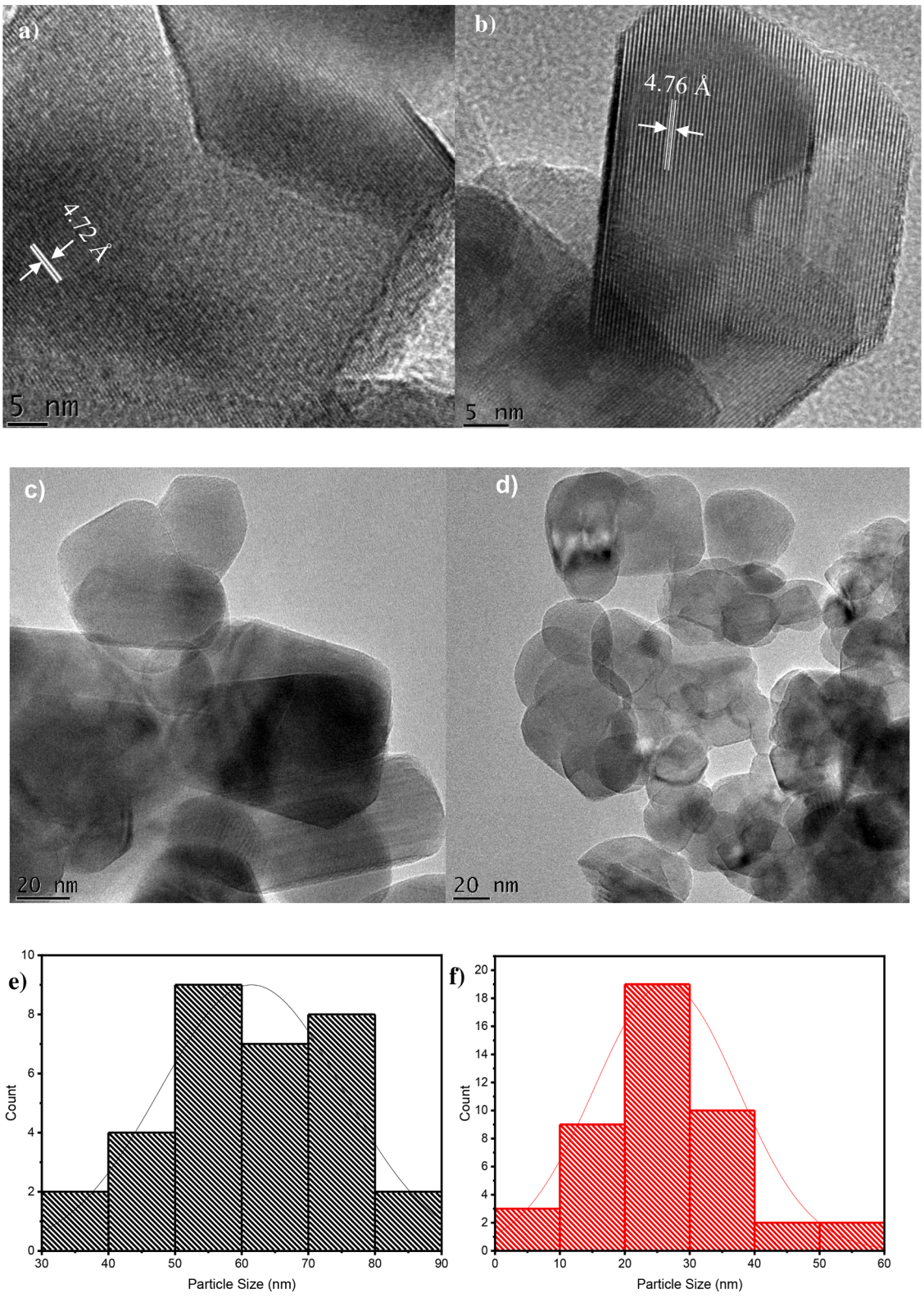

Fig. 7. TEM Micrographs of a) & c) Li_2MnO_3 and b) & d) $Li_2Mn_{0.95}Eu_{0.05}O_3$. Particle size distribution histogram of e) Li_2MnO_3 and f) $Li_2Mn_{0.95}Eu_{0.05}O_3$.

materials, and has been linked to improved porosity which could lead to enhanced performance of cathode materials due to increased surface area and shorter Li^+diffusion pathways.

EDX was used to determine the elemental composition of the synthesized nanostructured materials. EDX Spectra of Li_2MnO_3 and $Li_2Mn_{0.95}Eu_{0.05}O_3$ in Fig. 6(c) and (d) show the presence of all expected element i.e., Mn, O and Mn, Eu, O respectively, confirming formation of the desired materials. The absence of Li in the spectra is because of the inability of EDX to detect elements lighter than boron due to their low energy of characteristic radiation [29]. Table 2 shows that the Mn content of $Li_2Mn_{0.95}Eu_{0.05}O_3$ was lower than that of the pristine material indicating successful partial substitution of Mn with Eu. Moreover,

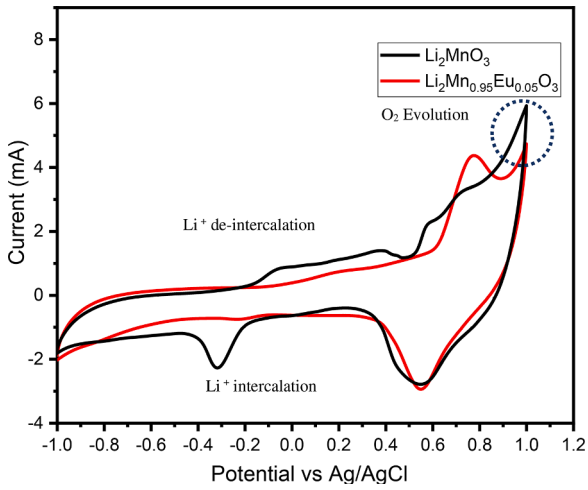

Fig. 8. Cyclic voltammograms of Li_2MnO_3 and $Li_2Mn_{0.95}Eu_{0.05}O_3$ in 1 M Li_2SO_4 electrolyte at 10 mVs^{-1} scan rates.

$Li_2Mn_{0.95}Eu_{0.05}O_3$ shows a lower O content which could be linked to oxygen vacancies within the synthesized material induced by doping as evidenced by the PXRD results in Fig. 1.

HR-TEM images of Li_2MnO_3 and $Li_2Mn_{0.95}Eu_{0.05}O_3$ presented in Fig. 7(c) and (d) respectively show the particle size and shape of the synthesized materials. Both images show quasi-spherical and nano-cube type crystallite shapes, with varying crystallite sizes. Fig. 7(e) and (f) show the particle size distributions for Li_2MnO_3 and $Li_2Mn_{0.95}Eu_{0.05}O_3$ respectively. $Li_2Mn_{0.95}Eu_{0.05}O_3$ exhibited much smaller particle sizes and a more uniform size distribution which is in good agreement with the PXRD and HR-SEM data. The particles are further characterized by agglomeration, which is attributed to the EDTA chelating agent, an observation also supported by HR-SEM images in Fig. 6. HR-TEM image in Fig. 7(a) and (b) with lattice fringes were processed using Image J software to determine the interplanar spacing of the Li_2MnO_3 and $Li_2Mn_{0.95}Eu_{0.05}O_3$ respectively. The interplanar spacing in Li_2MnO_3 and $Li_2Mn_{0.95}Eu_{0.05}O_3$ was determined to be 4.72 Å and 4.761 Å respectively, indicating that Eu-doping expanded the cell lattice due to its larger ionic radius. Furthermore, the interplanar spacing of both materials was found to be in the range of reported values [51–54] and correspond to the (100) direction of Li_2MnO_3 crystal.

3.4. Electrochemical characterization

To interrogate the reversibility of Li^+ intercalation kinetics, cyclic voltammetry was employed as seen in Fig. 8. The sharp "horn like" cathodic peak at ~ 1 V corresponded to activation of the materials which is characterized by oxygen evolution and the extraction of Li^+ in the form of Li_2O to form the more electrochemically active MnO_2 structure [55–57]. Moreover, the cyclic voltammogram of Li_2MnO_3 exhibits a larger additional redox pair ~ −0.3/−0.1 V corresponding to Li^+ de-intercalation and intercalation in the newly formed spinel structure [55].

The activation of Li_2MnO_3 materials by O_2 removal generated oxygen vacancies in the material and led to irreversible capacity loss in the first cycle as depicted in Fig. 8 [58]. On the other hand, the O_2 removal in the $Li_2Mn_{0.95}Eu_{0.05}O_3$ is much less defined and shows a lower intensity. This is a good indication that Eu doping stabilizes the lattice oxygen and thus prevents irreversible capacity loss during first cycling as depicted in Fig. 8 [55]. The lattice oxygen stabilization effect of Eu-doping further prevents the migration of the manganese ions previously coordinated to the released lattice oxygen, into vacant octahedral site that were occupied by the removed Li^+ [59]. The dissolution and migration of manganese from the TM layer into the Li layer leads to the formation of a spinel phase, slower lithium-ion movement and gradual fading of voltage during cycling [60]. The cyclic voltammogram of $Li_2Mn_{0.95}Eu_{0.05}O_3$ is further characterized by more symmetrical and defined redox peaks at ~ 0.58/0.75 V corresponding to Li^+ de-intercalation and intercalation. This is a good indication that Eu

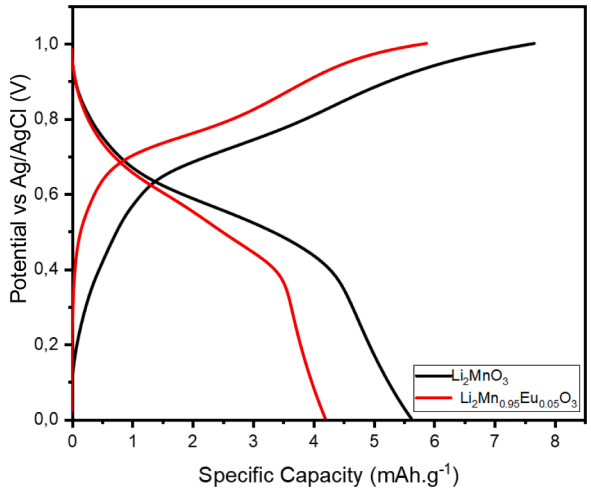

Fig. 10. 1st Charge-discharge voltage profiles of Li_2MnO_3 and $Li_2Mn_{0.95}Eu_{0.05}O_3$ at current density of 1 $A.g^{-1}$.

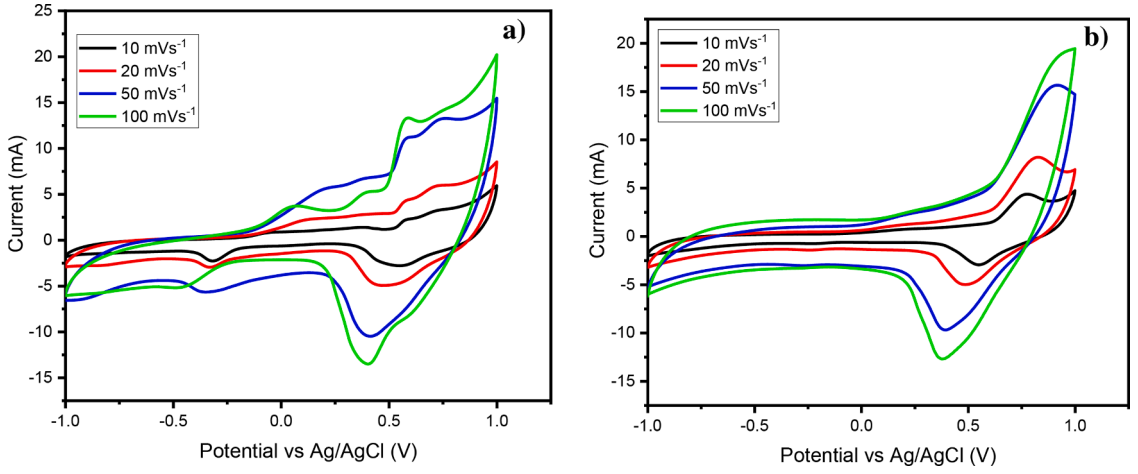

Fig. 9. Cyclic voltammograms of (a) Li_2MnO_3 and (b) $Li_2Mn_{0.95}Eu_{0.05}O_3$ in 1 M Li_2SO_4 electrolyte at various scan rates.

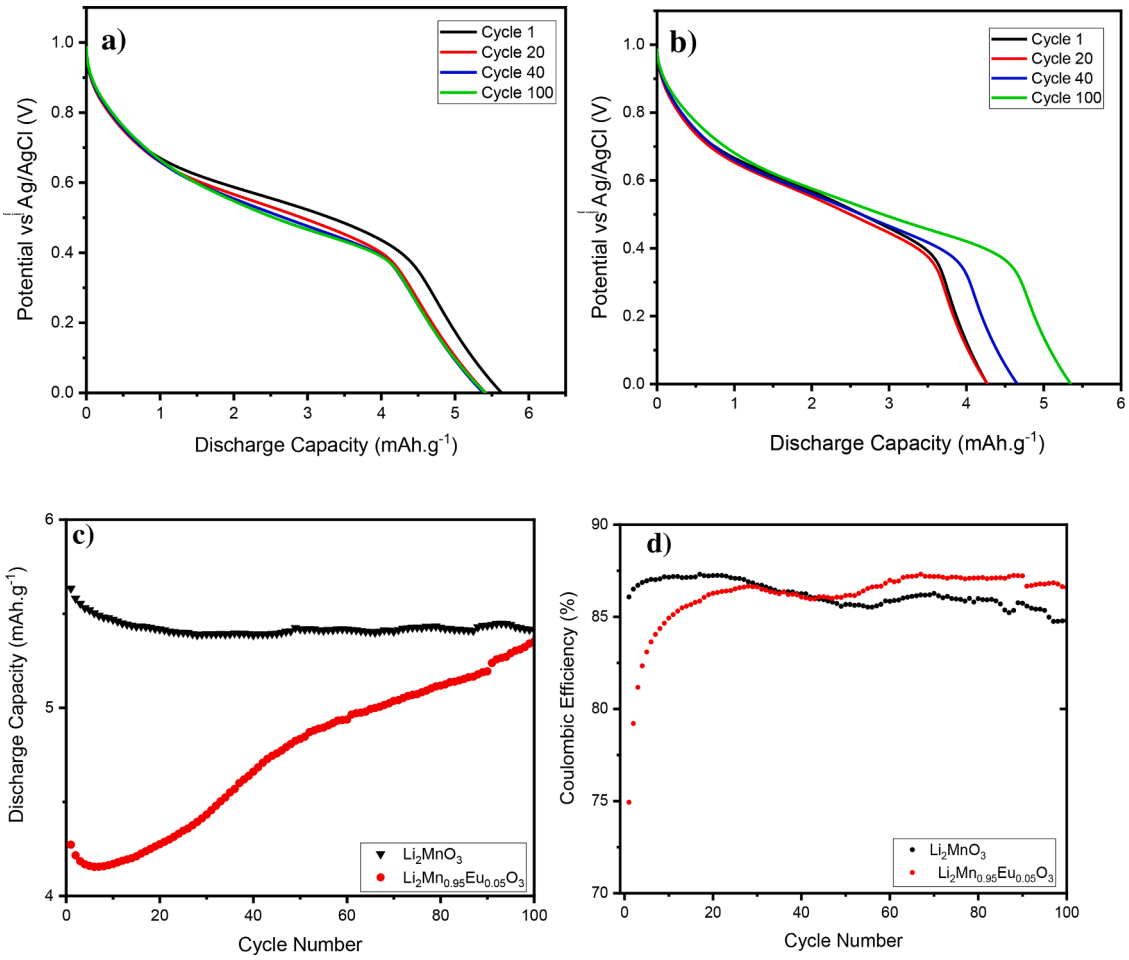

Fig. 11. Discharge voltage profiles of a) Li_2MnO_3 and b) $Li_2Mn_{0.95}Eu_{0.05}O_3$ after cycling at current density of 1 $A.g^{-1}$. c) Cycling performance of Li_2MnO_3 and $Li_2Mn_{0.95}Eu_{0.05}O_3$ over 100 cycles at current density of 1 $A.g^{-1}$ and d) Coulombic efficiency.

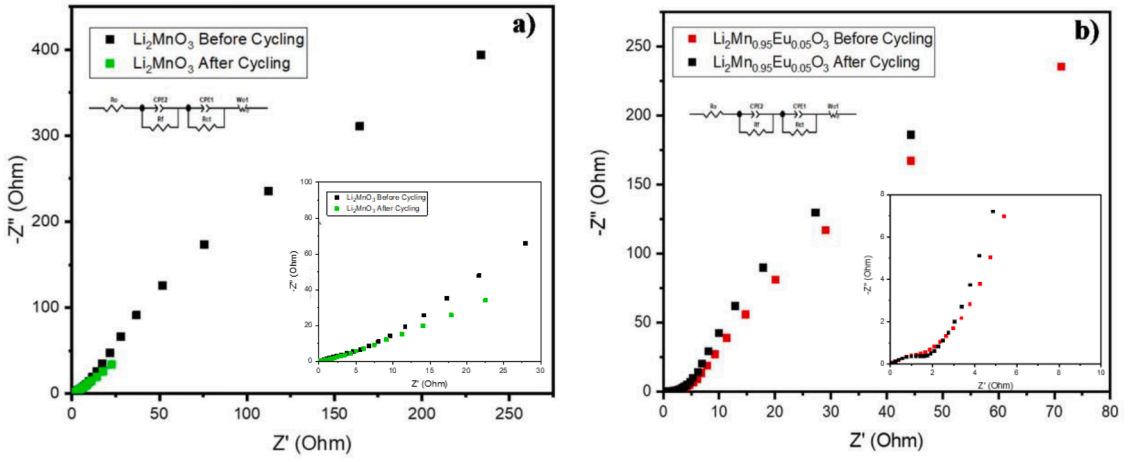

Fig. 12. Electrochemical impedance spectroscopy Nyquist plot of (a) Li_2MnO_3 and (b) $Li_2Mn_{0.95}Eu_{0.05}O_3$ before cycling.

doping induces improved reversibility and better degree of ordering at the Li^+ site [60]. This further provides evidence that $Li_2Mn_{0.95}Eu_{0.05}O_3$ is more structurally superior and slows down layered to spinel phase transformation which may lead to better cycling performance. The cyclic voltammograms in Fig. 8 were further employed to determine the specific capacities using Eq. (2) [61]:

$$\frac{\int IdV}{m \times \upsilon} \tag{2}$$

where $\int IdV$ is the integration of the area of the cyclic voltammogram, m is the mass in grams and ν is the scan rate in $mV.s^{-1}$. From Eq. (2), we have determined that the specific capacities of Li_2MnO_3 and $Li_2Mn_{0.95}Eu_{0.05}O_3$ is 27.78 $mAh.g^{-1}$ and 22.66 $mAh.g^{-1}$ respectively. The

Table 3
Electrochemical impedance spectroscopy parameters of Li_2MnO_3 and $Li_2Mn_{0.95}Eu_{0.05}O_3$ before and after cycling.

Parameter	Li_2MnO_3		$Li_2Mn_{0.95}Eu_{0.05}O_3$	
	1st Cycle	100th Cycle	1st Cycle	100th Cycle
R_s (Ohm)	2.586	4.464	2.826	2.669
R_{SEI} (Ohm)	0.23673	0.903	9.591	2.381
R_{ct} (Ohm)	1176	1211	936.1	206.8

lower initial specific capacity of $Li_2Mn_{0.95}Eu_{0.05}O_3$ can be attributed to a slower activation process due to the slower removal of lattice oxygen. Li_2MnO_3 and $Li_2Mn_{0.95}Eu_{0.05}O_3$ were further subjected to various scan rates to determine the effect of the scan rate on the electrochemistry as shown in Fig. 9. Even at higher scan rates both materials still maintained the same peaks indicating good reversibility.

To determine the discharge capacities of the pristine Li_2MnO_3 and $Li_2Mn_{0.95}Eu_{0.05}O_3$, galvanostatic charge-discharge measurements were performed as depicted in Fig. 10. The discharge capacities of Li_2MnO_3 and $Li_2Mn_{0.95}Eu_{0.05}O_3$ at a current density of 1 $A.g^{-1}$ were determined to be 5.63 $mAh.g^{-1}$ and 4.20 $mAh.g^{-1}$ respectively, with the latter showing that Eu doping slightly decreases the discharge capacity. The decrease in capacity is related to the activation of Li_2MnO_3 materials, which involved the removal of lithium from the structure as given in Eq. (3) [26]:

$$Li_2MnO_3 \rightarrow Li_2O + MnO_2 \quad (3)$$

The activation process is reported to be slower in $Li_2Mn_{0.95}Eu_{0.05}O_3$ ($x \geq 0.05$) materials and requires more charge-discharge cycles to improve [55]. The above observation is further supported by cyclic voltammetry data of $Li_2Mn_{0.95}Eu_{0.05}O_3$ which indicates a much less intense peak of Li_2O removal, and the discharge voltage profiles in Fig. 10 of $Li_2Mn_{0.95}Eu_{0.05}O_3$ at current density of 1 $A.g^{-1}$. This is taken as further evidence that the doping slowed down the phase transformation.

Fig. 11(a) and (b) shows discharge voltage profiles of Li_2MnO_3 and $Li_2Mn_{0.95}Eu_{0.05}O_3$ after cycling at current density of 1 $A.g^{-1}$ respectively. It is observed that the discharge capacity of $Li_2Mn_{0.95}Eu_{0.05}O_3$ improved with cycling from 4.20 $mAh.g^{-1}$ to 5.47 $mAh.g^{-1}$ while the discharge capacity of the pristine Li_2MnO_3 deteriorated from 5.63 $mAh.g^{-1}$ to 5.41 $mAh.g^{-1}$ with cycling. As a result of faster phase transformation, the pristine material discharge capacity faded with cycling due to side parasitic reactions at the electrode/electrolyte interphase and manganese dissolution [57]. The cycling performance of the two cathode materials was tested over 100 cycles to interrogate the Eu-doping effect on the cycling as shown in Fig. 11(c). Excessive oxygen redox may lead to a high oxygen vacancy in Li_2MnO_3 resulting to the migration of the Mn ions, leading to structural deterioration and instability with cycling. However, substituting some of the Mn ions with other cations have been shown to increase the stability of the material leading to reduced Mn ion migration consequently resulting to enhanced capacity with cycling [62]. The data further proved that the discharge capacity of $Li_2Mn_{0.95}Eu_{0.05}O_3$ improves with cycling and surpasses the discharge capacity of Li_2MnO_3 at $\geq$ 100 cycles. From Fig. 11(d), it is observed that Eu doping has a positive effect on the coulombic efficiency of Li_2MnO_3 with an increase in efficiency from ~74% to ~88% over 100 cycles indicating improvement of reversibility with cycling. The higher coulombic efficiency in $Li_2Mn_{0.95}Eu_{0.05}O_3$ implies that electrode electrolyte side reaction or parasitic reactions have been greatly reduced by the Eu-doping. The enhancement in coulombic efficiency of $Li_2Mn_{0.95}Eu_{0.05}O_3$ can be attributed to the substitution of some Mn with Eu ions which slow down phase transformation and improved the material structural stability. Such improved performances were also observed with Al doping of Li_2MnO_3 ($Li_2Mn_{0.9}Al_{0.1}O_3$) by Xiang and Wu [31]. Their result indicated that the Al doping not only prevented the first charged phase transformation from a layered phase to a cubic spinel-like phase, but it also slowed down the rate of transformation upon cycling in addition to reducing the charge transfer resistance. Ni and Cr have also been used to used improve the electrochemical performance of Li_2MnO_3 [63, 64].

Comparative electrochemical impedance spectroscopy Nyquist plot of Li_2MnO_3 and $Li_2Mn_{0.95}Eu_{0.05}O_3$ before cycling are shown in Fig. 12. Both plots showed a semicircle within high and intermediate frequency region and a straight line in low frequency region. The intercept at high frequency corresponds to the ohmic resistance R_s. The diameter of the semicircle relates to the combination of surface-film resistance R_{SEI} and charge-transfer resistance R_{ct}, while the straight line is related to the diffusion-controlled process of lithium ions within the bulk. The EIS parameters of Li_2MnO_3 and $Li_2Mn_{0.95}Eu_{0.05}O_3$ are given in table 3. From the table, we observe that the charge transfer resistance of Li_2MnO_3 increased with cycling from 1176 to 1211 Ohm, as compared to $Li_2Mn_{0.95}Eu_{0.05}O_3$ where the resistance shows a decrease of 729.3 Ohm with cycling. This indicates that Eu doping induces increased conductivity with cycling.

4. Conclusion

Li_2MnO_3 and Eu-doped Li_2MnO_3 were successfully synthesized via sol-gel method. The synthesized Eu-doped material was given the formula $Li_2Mn_{0.95}Eu_{0.05}O_3$, which is consistent with stoichiometric data obtained from ICP-OES. Electrochemical studies to investigate the effect of Eu-doping on Li_2MnO_3 revealed that Eu-doping had the following synergistic effects: (1) reduced 1st cycle irreversible capacity loss by stabilizing the lattice oxygen (2) slowed down phase transformation with cycling by reducing the dissolution and migration of manganese ions into vacant octahedral site that were occupied by the removed Li^+ (3) improved the coulombic efficiency of Li_2MnO_3 due to improvement in the reversibility caused by reduced side or parasitic reactions as well as reduced phase transformations. Therefore, we can conclude that $Li_2Mn_{0.95}Eu_{0.05}O_3$ has good merits for application as a cathode material in aqueous based Li-ion battery systems.

CRediT authorship contribution statement

TumisoE Mabokela: Methodology, Investigation, Writing – original draft. **Assumpta C Nwanya:** Validation, Investigation, Writing – original draft, Writing – review & editing, Data curation. **Miranda M Ndipingwi:** Investigation, Writing – original draft, Data curation, Software. **Sodiq T Yussuf:** Data curation, Visualization, Writing – review & editing. **Precious I Ekwere:** Supervision, Software. **Onyinyechi V Uhuo:** Validation, Investigation. **Chinwe O Ikpo:** Validation, Investigation. **Kwena D Modibane:** Data curation, Writing – review & editing. **Emmanuel I Iwuoha:** Conceptualization, Project administration, Resources, Funding acquisition, Supervision, Writing – review & editing.

Declaration of Competing Interest

The authors hereby declare that the work is original, not under consideration for publication elsewhere and there is no conflict of interest.

Data availability

Data will be made available on request.

Acknowledgements

This work was funded by: (i) the South African Department of Science and Innovation (DSI) National Nanoscience Postgraduate Teaching and Training Platform (NNPTTP) Grant No. DST/CON 0025/2011–2021; and (ii) the National Research Foundation (NRF) of South

Africa Research Chair Initiative (SARChI) Grant No. 85102.

Supplementary materials

Supplementary material associated with this article can be found, in the online version, at doi:10.1016/j.electacta.2023.141865.

References

[1] O.J. Akintande, O.E. Olubusoye, A.F. Adenikinju, B.T. Olanrewaju, Modeling the determinants of renewable energy consumption: evidence from the five most populous nations in Africa, Energy 206 (2020), 117992.

[2] P.A. Owusu, S. Asumadu-Sarkodie, A review of renewable energy sources, sustainability issues and climate change mitigation, Cogent Eng. 3 (1) (2016), 1167990.

[3] H.Y. Tiantian Zhang, Chapter 7—high Efficiency Plants and Building Integrated Renewable Energy systems. *Handbook of Energy Efficiency in Buildings*, Butterworth-Heinemann, 2019, pp. 441–595.

[4] V.Y. Patade, L.C. Meher, A. Grover, S.M. Gupta, M. Nasim, Omics approaches in biofuel technologies: toward cost effective, eco-friendly, and renewable energy, In Omics Technol. Bio-Eng. (2018) 337–351. Academic Press.

[5] M.K. Islam, H. Wang, S. Rehman, C. Dong, H.Y. Hsu, C.S.K. Lin, S.Y. Leu, Sustainability metrics of pretreatment processes in a waste derived lignocellulosic biomass biorefinery, Bioresour. Technol. 298 (2020), 122558.

[6] H. Wu, J. Xiao, S. Hao, R. Yang, P. Dong, L. Han, M. Li, F. Yu, Y. Xie, J. Ding, Y. Zhang, In-situ catalytic gasification of kelp-derived biochar as a fuel for direct carbon solid oxide fuel cells, J. Alloys Compd. 865 (2021), 158922.

[7] K. Vohra, A. Vodonos, J. Schwartz, E.A. Marais, M.P. Sulprizio, L.J. Mickley, Global mortality from outdoor fine particle pollution generated by fossil fuel combustion: results from GEOS-Chem, Environ. Res. 195 (2021), 110754.

[8] K.B. Karnauskas, S.L. Miller, A.C. Schapiro, Fossil fuel combustion is driving indoor CO_2 toward levels harmful to human cognition, Geohealth 4 (5) (2020), e2019GH000237.

[9] J. Ghobadi, D. Ramirez, S. Khoramfar, R. Jerman, M. Crane, K. Hobbs, Simultaneous absorption of carbon dioxide and nitrogen dioxide from simulated flue gas stream using gas-liquid membrane contacting system, Int. J. Greenhouse Gas Control 77 (2018) 37–45.

[10] X. Jie, S. Gonzalez-Cortes, T. Xiao, B. Yao, J. Wang, D.R. Slocombe, Y. Fang, N. Miller, H.A. Al-Megren, J.R. Dilworth, J.M. Thomas, The decarbonisation of petroleum and other fossil hydrocarbon fuels for the facile production and safe storage of hydrogen, Energy Environ. Sci. 12 (1) (2019) 238–249.

[11] K. Alper, K. Tekin, S. Karagöz, A.J. Ragauskas, Sustainable energy and fuels from biomass: a review focusing on hydrothermal biomass processing, Sustainable Energy Fuels 4 (9) (2020) 4390–4414.

[12] R. Saroha, A.K. Panwar, A. Gaur, Y. Sharma, V. Kumar, P.K. Tyagi, Electrochemical studies of novel olivine-layered ($LiFePO_4$-Li_2MnO_3) dual composite as an alternative cathode material for lithium-ion batteries, J. Solid State Electrochem. 22 (8) (2018) 2507–2513.

[13] Y. Zuo, B. Li, N. Jiang, W. Chu, H. Zhang, R. Zou, D. Xia, A high-capacity O_2-type Li-rich cathode material with a single-layer Li_2MnO_3 superstructure, Adv. Mater. 30 (16) (2018), 1707255.

[14] V. Vega-Garita, A. Hanif, N. Narayan, L. Ramirez-Elizondo, P. Bauer, Selecting a suitable battery technology for the photovoltaic battery integrated module, J. Power Sources 438 (2019), 227011.

[15] A. Perner, J. Vetter, Lithium-ion batteries for hybrid electric vehicles and battery electric vehicles. Advances in Battery Technologies For Electric Vehicles, Woodhead Publishing, 2015, pp. 173–190.

[16] J. Falk, A. Nedjalkov, M. Angelmahr, W. Schade, Applying Lithium-Ion Second Life Batteries for Off-Grid Solar Powered System—A Socio-Economic Case Study for Rural Development, Zeitschrift für Energiewirtschaft 44 (1) (2020) 47–60.

[17] A.S. Ninawe, S.T. Indulkar, A. Amin, Impact of climate change on fisheries. Biotechnology For Sustainable Agriculture, Woodhead Publishing, 2018, pp. 257–280.

[18] T. Chen, Y. Jin, H. Lv, A. Yang, M. Liu, B. Chen, Y. Xie, Q. Chen, Applications of lithium-ion batteries in grid-scale energy storage systems, Trans. Tianjin Univ. 26 (3) (2020) 208–217.

[19] B. Diouf, R. Pode, Potential of lithium-ion batteries in renewable energy, Renew. Energy 76 (2015) 375–380.

[20] F.F. Bazito, R.M. Torresi, Cathodes for lithium ion batteries: the benefits of using nanostructured materials, J. Braz. Chem. Soc. 17 (4) (2006) 627–642.

[21] N. Nitta, F. Wu, J.T. Lee, G. Yushin, Li-ion battery materials: present and future, Mater. Today 18 (5) (2015) 252–264.

[22] T.E. Mabokela, A.C. Nwanya, M.M. Ndipingwi, S. Kaba, P. Ekwere, S.T. Werry, C. Ikpo, M. Kwena, E. Iwuoha, Recent advances on high-capacity li ion-rich layered manganese oxide cathodes, J. Electrochem. Soc. 168 (2021), 070530.

[23] Ehi-Eromosele, C.O., Ajayi, S.O. and Onwucha, C.N., Influence of fuels in the sol-gel combustion synthesis of Li2MnO3 positive electrode material for Li-ion battery. *Mater. Chem. Phys.,* 259, p. 124055.

[24] A.S. Menon, D.O. Ojwang, T. Willhammar, V.K. Peterson, K. Edstrom, C.P. Gomez, W.R. Brant, Influence of synthesis routes on the crystallography, morphology, and electrochemistry of Li_2MnO_3, ACS Appl. Mater. Interfaces 12 (5) (2020) 5939–5950.

[25] Z. Moradi, A. Heydarinasab, F. Pajoum Shariati, First-principle study of doping effects (Ti, Cu, and Zn) on electrochemical performance of Li_2MnO_3 cathode materials for lithium-ion batteries, Int. J. Quantum Chem. (2020) 26458.

[26] C. Jacob, J. Jian, Q. Su, S. Verkhoturov, R. Guillemette, H. Wang, Electrochemical and structural effects of in situ Li_2O extraction from Li_2MnO_3 for Li-ion batteries, ACS Appl. Mater. Interfaces 7 (4) (2015) 2433–2438.

[27] A. Lanjan, B.G. Choobar, S. Amjad-Iranagh, First principle study on the application of crystalline cathodes $Li_2Mn_{0.5}TM_{0.5}O_3$ for promoting the performance of lithium-ion batteries, Comput. Mater. Sci. 173 (2020), 109417.

[28] A. Abulikemu, T. Matsunaga, A. Watanabe, K. Yamamoto, T. Uchiyama, K. Nakanishi, S. Kawaguchi, K. Osaka, Y. Uchimoto, Rocksalt type $Li_2Nb_{0.15}Mn_{0.85}O_3$ without structure degradation or redox evolution upon cycling, J. Alloys Compd. 853 (2021), 156984.

[29] T.R. Somo, T.E. Mabokela, D.M. Teffu, T.K. Sekgobela, B. Ramogayana, M.J. Hato, K.D. Modibane, A comparative review of metal oxide surface coatings on three families of cathode materials for lithium ion batteries, Coatings 11 (7) (2021) 744.

[30] W. Zhao, L. Xiong, Y. Xu, X. Xiao, J. Wang, Z. Ren, Magnesium substitution to improve the electrochemical performance of layered Li_2MnO_3 positive-electrode material, J. Power Sources 330 (2016) 37–44.

[31] Y. Xiang, X. Wu, Enhanced electrochemical performances of Li_2 MnO_3 cathode materials by Al doping, Ionics (Kiel) 24 (1) (2018) 83–89.

[32] K. Shimoda, K. Yazawa, T. Matsunaga, M. Murakami, K. Yamanaka, T. Ohta, E. Matsubara, Z. Ogumi, T. Abe, Sequential delithiationbehavior and structural rearrangement of a nanoscale composite-structured $Li_{1.2}Ni_{0.2}Mn_{0.6}O_2$ during charge–discharge cycles, Sci. Rep. 10 (1) (2020) 1–12.

[33] Y. Gao, J. Ma, X. Wang, X. Lu, Y. Bai, Z. Wang, L. Chen, Improved electron/Li-ion transport and oxygen stability of Mo-doped Li_2MnO_3, J. Mater. Chem. A 2 (13) (2014) 4811–4818.

[34] X. Li-Long, X. Xiang, X. You-Long, W. Ji-Sheng, Syntheses and electrochemical characterization of Li-Rich $Li_2Mn_{1-x}Ti_xO_3$ layered materials used for lithium ion batteries, Chin. J. Inorg. Chem. 33 (2) (2017) 269–275.

[35] W. Wei, Q. Xing, G. Jianling, W. Jiangfeng, Y. Huiyu, W. Li, Influence of cerium doping on structure and electrochemical properties of $LiNi_{0.5}Mn_{1.5}O_4$ cathode materials, J. Rare Earths 35 (9) (2017) 887–895.

[36] P. Luo, Z. Huang, Fabrication of scandium-doped lithium manganese oxide as a high-rate capability cathode material for lithium energy storage, Solid State Ionics 338 (2019) 20–24.

[37] C. Zhu, J. Liu, X. Yu, Y. Zhang, P. Dong, X. Wang, Y. Zhang, Boosting the stable Li storage performance in one-dimensional $LiLa_xMn_{2-x}O_4$ nanorods at elevated temperature, Ceram. Int. 45 (15) (2019) 19351–19359.

[38] P. Ram, A. Gören, S. Ferdov, M.M. Silva, R. Singhal, C.M. Costa, R.K. Sharma, S. Lanceros-Méndez, Improved performance of rare earth doped $LiMn_2O_4$ cathodes for lithium-ion battery applications, New J. Chem. 40 (7) (2016) 6244–6252.

[39] G. Çelik, S. Aktaş, Ş. Ateş, O.M. Özkendir, W. Klysubun, Crystal and electronic structure study of the $Li_2Mn_{1-x}Nd_xO_3$ battery cathode, Progr. Nat. Sci.: Mater. Int. 29 (2) (2019) 119–123.

[40] A. Yuzer, O.M. Ozkendir, Influence of rare-earth substitution on the crystal and electronic properties of a Li_2MnO_3 battery cathode, J. Electron. Mater. 45 (2) (2016) 989–998.

[41] Z. Lu-Min, Z. Shu-Ping, X. Bo, O. Chu-Ying, First-principles study of rare-earth-doped cathode materials Li_2MnO_3 in Li-ion batteries, Acta PhysicaSinica 68 (13) (2019) 1–9, 2019.

[42] S. Muhammad, S. Yun, K. Palanisamy, H. Kim, W.S. Yoon, Mechanistic studies on reversible conversion reaction in Li_2MnO_3-carbon nanotube composite anode, J. Power Sources 423 (2019) 323–330.

[43] F.A. Susai, M. Talianker, J. Liu, T. Paul, Y. Grinblat, E. Erickson, M. Noked, L. Burstein, A.I. Frenkel, Y. Tsur, B. Markovsky, Electrochemical activation of Li_2MnO_3 electrodes at 0°C and its impact on the subsequent performance at higher temperatures, Materials (Basel) 13 (19) (2020) 4388.

[44] Y. Li, F. Wang, H. Zhai, D. Wang, N. Yang, S. Chen, K. Chen, Improving the electrochemical performance of Li_2MnO_3 cathode material by micro-substitution of nickel to manganese, Ionics (Kiel) 26 (2) (2020) 683–690.

[45] Q. Ma, R. Li, R. Zheng, Y. Liu, H. Huo, C. Dai, Improving rate capability and decelerating voltage decay of Li-rich layered oxide cathodes via selenium doping to stabilize oxygen, J. Power Sources 331 (2016) 112–121.

[46] B.H. Toby, R.B. Von Dreele, GSAS-II: the genesis of a modern open-source all-purpose crystallography software package, J. Appl. Crystallogr. 46 (2) (2013) 544–549.

[47] M. Jansen, R. Hoppe, On the knowledge of the NaCl family of structures: new studies on Li_2MnO_3, Z. Anorg. Allg. Chem. 397 (3) (1973) 279–289.

[48] Z. Yu, J. Hao, W. Li, H. Liu, Enhanced electrochemical performances of cobalt-doped Li_2MoO_3 cathode materials, Materials (Basel) 12 (6) (2019) 843.

[49] Q. Zhang, T. Peng, D. Zhan, X. Hu, Synthesis and electrochemical property of $xLi_2MnO_3{\cdot}(1-x)LiMnO_2$ composite cathode materials derived from partially reduced Li_2MnO_3, J. Power Sources 250 (2014) 40–49.

[50] M. Ranjeh, M. Masjedi-Arani, M. Salavati-Niasari, H. Moayedi, EDTA-modified sol-gel synthesis of monoclinic Li_2MnO_3 nanoparticles as an effective photocatalyst for degradation of organic dyes, J. Mol. Liq. 300 (2020), 112292.

[51] W. Zhao, L. Xiong, Y. Xu, H. Li, Z. Ren, High performance Li_2MnO_3/rGO composite cathode for lithium ion batteries, J. Power Sources 349 (2017) 11–17.

[52] X. Lan, Y. Xin, L. Wang, X. Hu, Nanoscale surface modification of Li-rich layered oxides for high-capacity cathodes in Li-ion batteries, J. Nanopart. Res. 20 (3) (2018) 80.

[53] J.E. Lee, M.C. Kim, S.H. Moon, E.S. Kim, Y.K. Shin, S. Choi, S.H. Kwon, S.J. Kim, H. J. Kwon, K.W. Park, Role of polyvinylpyrrolidone in the electrochemical

performance of Li_2MnO_3 cathode for lithium-ion batteries, RSC Adv. 9 (18) (2019) 10297–10304.
[54] G. Hu, Z. Xue, W. Wang, F. Zhu, Q. Sun, J. Huang, Z. Peng, Y. Cao, K. Du, A facile synthesis approach of Li_2MnO_3 cathode material for lithium-ion battery by one-step high-energy mechanical activation method, Mater. Technol. (2020) 1–6.
[55] P.P. Dahiya, C. Ghanty, K. Sahoo, S. Basu, S.B. Majumder, Suppression of voltage decay and improvement in electrochemical performance by zirconium doping in Li-rich cathode materials for Li-ion batteries, J. Electrochem. Soc. 165 (13) (2018) A3114.
[56] W. Tang, Y. Zhu, Y. Hou, L. Liu, Y. Wu, K.P. Loh, H. Zhang, K. Zhu, Aqueous rechargeable lithium batteries as an energy storage system of superfast charging, Energy Environ. Sci. 6 (7) (2013) 2093–2104.
[57] G.J. Wang, L.J. Fu, B. Wang, N.H. Zhao, Y.P. Wu, R. Holze, An aqueous rechargeable lithium battery based on LiV_3O_8 and $Li[Ni_{1/3}Co_{1/3}Mn_{1/3}]O_2$, J. Appl. Electrochem. 38 (4) (2008) 579–581.
[58] M. Freire, O.I. Lebedev, A. Maignan, C. Jordy, V. Pralong, Nanostructured Li_2MnO_3: a disordered rock salt type structure for high energy density Li ion batteries, J. Mater. Chem. A 5 (41) (2017) 21898–21902.
[59] F. Ding, J. Li, F. Deng, G. Xu, Y. Liu, K. Yang, F. Kang, Surface heterostructure induced by $PrPO_4$ modification in $Li_{1.2}[Mn_{0.54}Ni_{0.13}Co_{0.13}]O_2$ cathode material for high-performance lithium-ion batteries with mitigating voltage decay, ACS Appl. Mater. Interfaces 9 (33) (2017) 27936–27945.
[60] T.F. Yi, Y.R. Zhu, X.G. Hu, Structure and electrochemical properties of $LiLa_xMn_{2-x}O_4$ cathode material by the ultrasonic-assisted sol-gel method, Int. J. Minerals Metallurg. Mater. 16 (1) (2009) 119–123.
[61] S. Willenberg, N. Ross, Enhanced electrochemistry of carbon supported functionalized nanocomposite cathode for aqueous lithium-ion batteries, Electroanalysis 32 (12) (2020) 2976–2981.
[62] I.M. Nwachukwu, A.C. Nwanya, A.B.C. Ekwealor, F.I. Ezema, Recent progress in Mn and Fe-rich cathode materials used in Li-ion batteries, J. Energy Storage 54 (2022), 105248.
[63] G. Singh, R. Thomas, A. Kumar, R.S. Katiyar, Electrochemical behaviour of Cr-doped composite Li_2MnO_3-$LiMn_{0.5}Ni_{0.5}O_2$ cathode materials, J. Electrochem. Soc. 159 (4) (2012) A410.
[64] S. Jeong, K. Choi, V.-.C. Ho, J. Cho, J.-.S. Bae, S.C. Nam, T. Yim, J. Mun, Crucial role of Ni-doping to interfacial Li_2MnO_3 layer of High-performance Ni-rich layered cathode in Lithium-Ion batteries, Chem. Eng. J. 434 (2022), 134577.